Intensive processing optimization for achieving strong and ductile Al-Mn-Mg-Sc-Zr alloy produced by selective laser melting

D. Bayoumy [a,b], D. Schliephake [a,b,c], S. Dietrich [c], X.H. Wu [a,b], Y.M. Zhu [a,b,*], A.J. Huang [a,b,*]

[a] Monash Centre for Additive Manufacturing, 15-17 Normanby Rd, Notting Hill, VIC 3168, Australia
[b] Department of Materials Science and Engineering, Monash University, Clayton, VIC 3800, Australia
[c] Institute for Applied Materials (IAM-WK), Karlsruhe Insitute of Technology (KIT), Engelbert-Arnold-Straße 4, 76131 Karlsruhe, Germany

HIGHLIGHTS

- The optimum processing window for selective laser melted Al-Mn-Mg-Sc-Zr alloy has been established for the first time.
- Good combination of strength and ductility is attainable by using a wide range of laser energy inputs.
- The microstructure involves a unique bimodal grain structure and Al_3Sc and Mn(Fe)-rich quasicrystal phases.

GRAPHICAL ABSTRACT
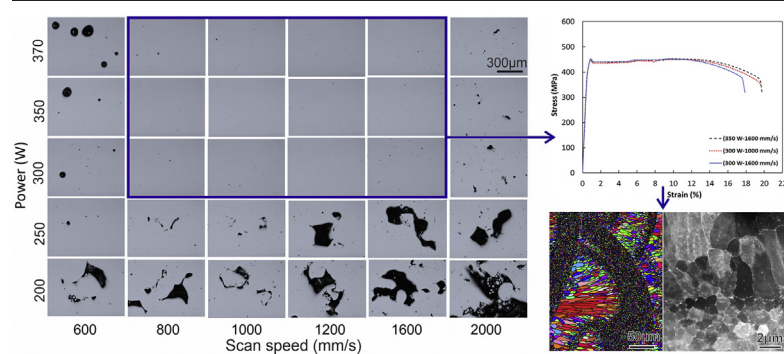
ARTICLE INFO

ABSTRACT

The Sc-containing Al—Mn alloy system produced by additive manufacturing (AM) has recently presented exciting new opportunities to achieve a step-change in mechanical properties, but its processability remains unclear. In this work, the optimum processing window for the Al-Mn-Mg-Sc-Zr alloy fabricated by selective laser melting (SLM) has been established for the first time. The window covers the range of processing parameters that can lead to a good combination of part density, strength, ductility, and processability. The alloys fabricated within this optimized processing window of SLM have the material relative density more than 99.8% with less porosity. Moreover, all these alloys have the yield strength exceeding 430 MPa and the ductility of over 17%. Further microstructural examinations suggest that such excellent mechanical properties are associated with a bimodal grain architecture. Also, a high number density of intermetallic particles has been detected in these two-grain regions. They are confirmed to be Al_3Sc and Mn(Fe)-rich quasicrystal. Most of these particles distributing along grain boundaries are expected to pin the grain boundaries and contribute to the high strength of this alloy. The findings will provide an essential basis for achieving exceptional mechanical performance and intricate geometry designs of the alloy using AM.

1. Introduction

Additive manufacturing (AM) technology for producing metallic parts is attracting global attention in recent years because it can achieve design freedom and structural optimization of products more efficiently than other traditional manufacturing techniques [1]. Among various AM technologies, the selective laser melting (SLM) has been regarded as

* Corresponding authors at: Monash Centre for Additive Manufacturing, 15-17 Normanby Rd, Notting Hill, VIC 3168, Australia.
E-mail addresses: yuman.zhu@monash.edu (Y.M. Zhu), aijun.huang@monash.edu (A.J. Huang).

one of the most promising processes to produce engineering components [2,3]. The rapid solidification nature of the SLM can generate a refined microstructure, leading to mechanical properties that are comparable to or even better than those of traditional cast or wrought products [4]. Also, SLM can promote cleaner production by saving raw materials and reducing production time [5]. Owing to these advantages, SLM has been applied to various metal material systems, such as Ti alloys [6], Fe-based materials [7], Ni [8] and Co alloys [9], and Al alloys [10–12]. Among these alloy systems, Al alloys built by SLM are receiving a growing demand from aerospace industries to realize the lightweight of components with near-net shape [3]. Till now, the most widely used Al alloys for SLM are based on the Al—Si eutectic system (i.e., AlSi12, AlSi7Mg, and AlSi10Mg) due to their excellent weldability [2]. However, the fabricated products using these Al alloys usually exhibit limited and anisotropic mechanical properties [1,11–13]. This is mainly because of the extremely high thermal gradient in SLM that promotes the formation of coarse columnar grains growing along the building direction [3]. Besides, SLM fabrication of other Al alloys, such as 2000 and 7000 series, have also been explored. Nevertheless, most of them showed a severe hot tearing during the building process [14–20] due to the high solidification rate associated with the SLM [21].

Many previous studies have shown that scandium (Sc) is one of the most effective alloying elements in Al alloys, and its minor addition can significantly improve the mechanical properties of Al alloys [22–25]. Therefore, the applicability of SLM for modified Al alloys with Sc content has been explored in recent years [26–30]. Typically, a commercial alloy, designated Scalmalloy, which is a Sc-modified 5xxx Al alloy (i.e., Al-Mg-Sc-Zr), has been specifically developed for AM [31–33]. Owing to the addition of Sc, a yield strength of 290 MPa and an elongation exceeding 15% have been reported for the SLM-fabricated condition [33]. Further studies showed that the superior mechanical properties of Scalmalloy were due to the formation of a large area of ultra-fine, equiaxed grains that support material strength with low anisotropy compared to Al—Si alloys. A wide range of processing parameters have also been reported for the SLM-fabricated parts that were free of solidification cracks with density around 99.5% when laser energy density $\geq$ 135 J/mm^3 was used [34]. Very recently, a Sc-modified 3xxx alloy system, i.e., Al-Mn-Mg-Sc-Zr, has been designed for the SLM [35,36], which showed even better mechanical properties than the Scalmalloy. By applying a laser power of 370 W and a scan speed of 1000 mm/s, the recent study has reported a yield strength of 430 MPa with an elongation of 19% for this alloy. It was further found that such excellent mechanical properties were mainly offered by the Mn and Sc elements that contributed to the strength by solid solution strengthening and precipitation hardening.

Given the great potential of the SLM-fabricated Al-Mn-Mg-Sc-Zr alloy for industries (e.g. aerospace and automotive), the successful realization of this potential requires a deep understanding of the SLM process and limitations. The development of an appropriate processing window that enables high-quality parts with consistent properties is considered to be a key step for paving the way for AM industrialization. Till now, however, the reliable processing window for the SLM-fabricated Al-Mn-Mg-Sc-Zr alloy remains to be established. It is noted that the optimum processing parameters are particularly critical for the broad application of SLM-fabricated Al alloys in industries [1]. This is mainly because Al powder has inherently high reflectivity and high thermal conductivity, which will reduce the powder laser absorption [37,38]. Also, the formation of oxide layers on the melt pool promotes porosity formation [37]. The existence of pores and defects in parts produced by SLM usually depreciate the tensile properties and have detrimental effects on the fatigue properties [39]. Besides, entrapped gas pores and lack of fusion defects tend to form due to instability of molten pool and act as miniaturized notches that raise stress concentration and act as crack initiation sites [39,40]. Consequently, optimum processing parameters for minimizing defects is a preliminary but critical step for improving the mechanical performance and

ensuring the reproducibility of high-quality parts. Therefore, this work aims to establish the optimized range of processing parameters for the SLM production of the Al-Mn-Mg-Sc-Zr alloy. Furthermore, the material density, porosity, mechanical properties, and characteristic microstructure of the samples built within the optimum processing window will be evaluated and examined. The work is expected to provide an essential basis for producing net shape components with high quality and step-change mechanical performance to meet the increasing demand in industries.

2. Methods

2.1. Materials, processing and mechanical testing

Metal powders for the SLM were gas atomized out of the designed alloy composition, and their chemical composition was analyzed by inductively coupled plasma atomic emission spectroscopy (ICP-OES), as displayed in Table 1. A further scanning electron microscopy (SEM) examination shows that most of the powder particles have a nearly spherical shape (Fig. 1(a)). The particle size distribution was measured by laser diffraction technique using Malvern Mastersizer 2000. As shown in Fig. 1(b), the size of the powder is in the range of 20–70 μm with an average value of around 35 μm.

The SLM processing was carried out using a commercial EOS M290 powder-bed machine equipped with a Yb-fiber laser with a wavelength of 1060–1100 nm and a maximum power of 400 W (laser spot size: around 100 μm). Test cubes with the dimensions of $10 \times 10 \times 10$ mm^3 were built at various laser power and scan speed that range from 200 to 370 W and 600–2000 mm/s respectively for process optimization. For all the processing, the hatch distance was kept being 0.1 mm, while the powder layer thickness was 30 μm. All cubes were processed with a laser beam rotation of 67° alternating between consecutive layers. The processing was performed under a controlled Argon environment with a minimum oxygen level of 0.1 vol%. The relative density of the samples was averaged from three measurements using the Archimedes method [11,41].

Specimens for tensile mechanical testing were machined according to ASTM E8/E8M-16a. A room-temperature tensile test was performed using a 100 kN Instron 5982 machine at a strain rate of 0.015 min^{-1}. Three horizontal samples (with the tensile axis normal to the build direction) were tested for each condition to get an average result.

2.2. Microstructural characterization

2.2.1. X-ray micro-computed-tomography

The X-ray micro-computed-tomography (μ-CT) images for representative defect analysis of the samples were measured using a Zeiss Xradia 520 Versa μ-CT system. The μ-CT X-ray tube was operated at an acceleration voltage of 140 kV and a power of 10 W. The geometrical magnification of the system allowed for a pixel size of approx. 14.2 μm, the detector was used at an exposure time of 1 s for each projection. The 3D μ-CT tomograms were reconstructed from 1601 projections using Zeiss TXMReconstructor. Based on the reconstructed image slices, the image analysis software VGStudio MAX 3.3 (Volume Graphics GmbH, 2019) was used to determine the surface of the sample and thereby fixing the region of interest for porosity investigation. The image stack was then further processed for porosity detection using segmentation and labeling via VGStudio MAX 3.3 "VGEasyPore" algorithm. The VGEasyPore is a local contrast-based approach that can

Table 1
Chemical composition of alloy powder for SLM.

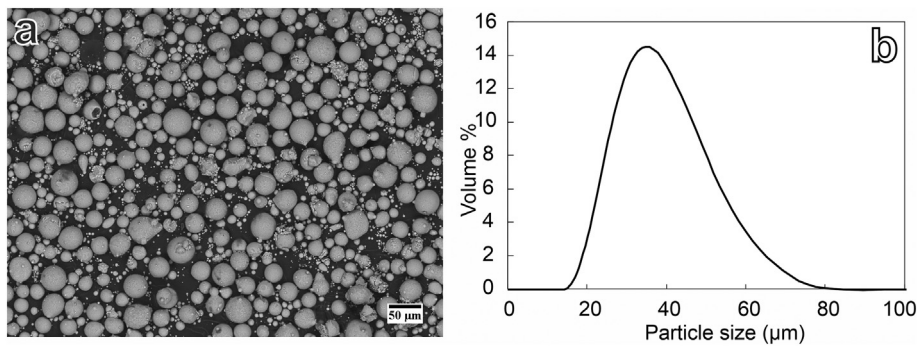| Element	Al	Mn	Mg	Sc	Zr	Fe	Si
Percentage (wt%)	Bal.	4.58	1.24	0.91	0.42	0.07	0.04

Fig. 1. (a) SEM image showing powder morphology and (b) particle size distribution.

handle grey value deviations in the material originating from scan artifacts, e.g., beam hardening and local noise or density variations. For the segmentation in VGEasyPore, a local region of 10 voxels and a contrast parameter of 3000 was chosen in the software settings for all specimens. The labeled pores were filtered by using a minimum volume of 8 voxels as a cut-off, which corresponding to 2.3E-5 mm^3.

The detected pores were visualized and analyzed using the VGStudio MAX 3.3 3D rendering capabilities to investigate morphological pore features of the different samples. As morphological features relevant for the current study, the diameter of the circumscribed sphere (pore diameter), the volume, and the sphericity was examined. The sphericity was used as a shape descriptor to indicate how spherical the pore is. Sphericity is defined as [42].

$$\Psi = \frac{\pi^{1/3}(6V)^{2/3}}{A} \tag{1}$$

where v is the volume of the pore, A is the surface area. Thus, Ψ can take values $0 < \Psi \leq 1$ ("1" represents a spherical pore, and "0" represents an elongated irregular pore). In this study, pores with sphericity <0.4 are referred to as irregular, while pores with sphericity >0.4 are referred to as regular.

2.2.2. Optical microscopy imaging

The samples for optical microscopy (OM) were mounted in epoxy resin, ground to 2400 Grit size, and polished using silica colloidal suspension. OM images were taken using a Nikon Eclipse light microscope and then analyzed by image analysis using ImageJ to estimate the percentage of porosity [43].

2.2.3. Scanning electron microscopy (SEM)

Samples for SEM were ground and then etched in a solution of 1% HF, 4% HNO$_3$, and 95% H$_2$O for 20 s to reveal the melt pool and grain boundaries. The backscattered electron (BSE) imaging and electron backscattered diffraction (EBSD) acquisition in SEM were undertaken using a field emission SEM JEOL 7001F equipped with Oxford instruments Nordlys Max2 EBSD detector. The EBSD data was acquired at an accelerating voltage of 20 kV and a step size of 0.15 μm and 0.02 μm for the large area and the fine grain region, respectively. The EBSD map of the fine grain region presented in Fig. 8(b) was captured in transmission EBSD (t-EBSD) mode. The sample preparation for t-EBSD consisted of cutting slices 0.3 mm in thickness, punched into 3 mm diameter discs, ground to ~50 μm thickness. The final thinning for the t-EBSD sample was made by low-angle ion milling using a Gatan Precision Ion Polishing System (PIPS I). All the EBSD data was analyzed using HKL Channel5 software.

The grain width in the coarse grain region is estimated from EBSD measurements of 5 subsets (each subset contains more than 600 grains). Fine-grain region area fraction was estimated from 10 BSE micrographs per processing condition (covering a total area of 1.13E

+06 μm^2) using BSE channeling contrast. The grain width in the fine grain region is estimated by the standard linear-intercept method from 10 BSE micrographs per processing condition (covering a total area of 1080 μm^2), using BSE channeling contrast assuming an equiaxed grain morphology.

2.2.4. Scanning transmission electron microscopy (STEM)

For scanning transmission electron microscopy (STEM), bulk samples were sliced into 0.3 mm thick pieces using a slow speed saw. These slices were punched into 3 mm diameter discs, ground to ~40 μm in thickness, and then followed by ion milling using a Gatan Precision Ion Polishing System (PIPS II). The STEM images were obtained using a FEI Titan 80–300 transmission electron microscope operating at 300 kV. The convergence semi-angle was set to a 15.0 mrad, leading to a probe diameter of ~0.12 nm. The bright-field (BF-) and low-angle annular dark-field (LAADF-) STEM images were collected in the (semi-) angle range of 0–10 mrad and 19–33 mrad, respectively. In high-angle annular dark-field (HAADF-) STEM imaging mode, the camera length was set to give an inner collection semi-angle of ~64 mrad. Energy-dispersive X-ray spectroscopy (EDXS) maps were obtained in STEM mode using the FEI Titan.

3. Results

3.1. Material density and porosity

The material density of the as-fabricated SLM samples that have been built in various scan speeds and laser powers was firstly examined, and the results are shown in Fig. 2. According to the figure, by applying laser power of 200 W, the material density maintains around 99% when the scan speed is between 600 mm/s and 1200 mm/s, but drops to 97.5% for the scan speed of 1600 mm/s. A similar trend applies to the laser power of 250 W, for which the material density increases to around 99.5% but quickly decreases at the scan speed of 1600 mm/s and over. When the laser power is above 250 W, i.e., 300 W, 350 W and 370 W, near fully dense samples (> 99.75%) can be constantly obtained for the scan speeds from 800 mm/s to 1600 mm/s. Based on these results, it seems that a denser material can be achieved by applying the higher laser power (300 W, 350 W and 370 W) in a wide range of scan speeds.

Having shown the material density of the samples printed in various conditions, we further examine the porosity in these samples. Fig. 3 provides a series of OM micrographs showing the amount, size, and morphology of pores existing in the microstructure of the samples with various laser power and scan speed. As shown by these images, the typical lack of fusion pores with an irregular shape are progressively formed with increasing scan speed for a constant laser power of 200 W and 250 W. They also form when laser power is higher than 300 W and scan speed is faster than 1600 mm/s. Their formation is most likely due to insufficient fusion at these low energy inputs. When the power increases to 300 W and above, the low scan speed of
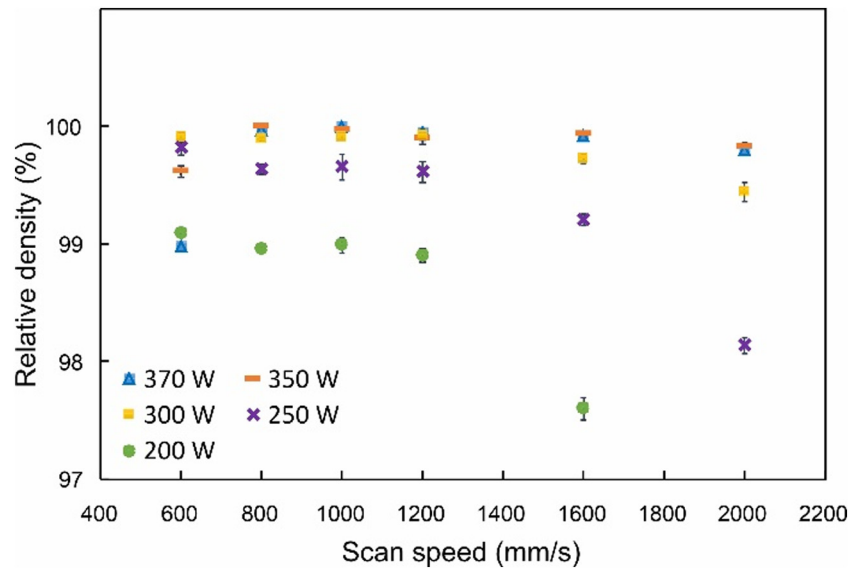
Fig. 2. Relative density of the as-fabricated Al-Mn-Mg-Sc-Zr alloy at various laser powers and scan speeds.
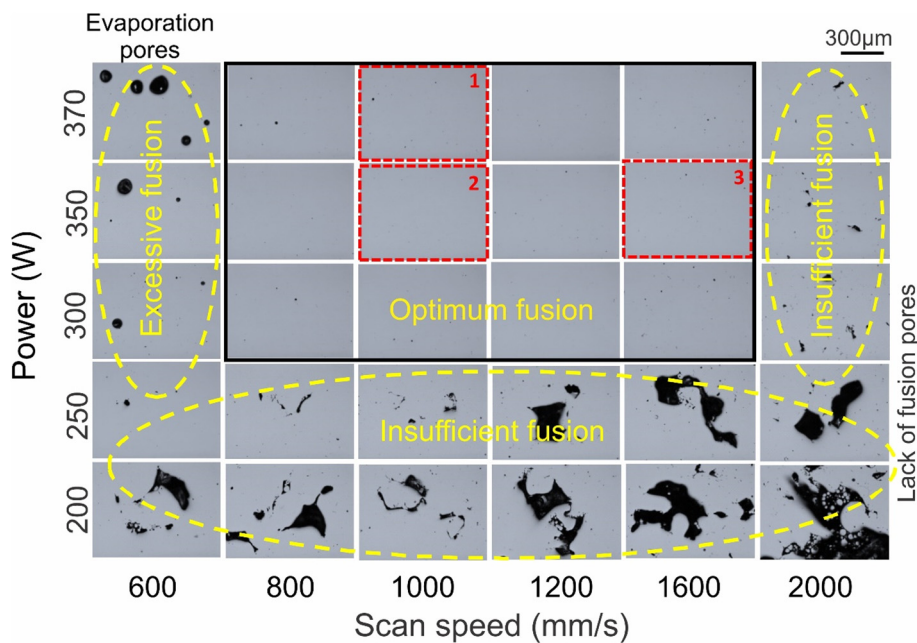

Fig. 3. Optical micrographs of Al-Mn-Mg-Sc-Zr samples showing the porosity at different laser power and scan speed. The optimum processing window is shown by a black-color solid-line frame. The processing parameters chosen for μ-CT image analysis are indicated by a red-color dashed-line frame.

600 mm/s leads to the formation of typical evaporation pores from excessive fusion. Such type of pores exhibits a near-round shape with the diameter larger than 100 μm. When the scan speed is higher than 600 mm/s, both the amount and size of these pores are reduced, especially in the scan speed range between 800 mm/s and 1600 mm/s, where only limited round pores with the size smaller than 100 μm were observed. Therefore, high consolidation samples with no significant metallurgical defects can be achieved in this scan speed range, as shown by the black solid-line frame in Fig. 3. We further performed image analyses for these images. The results revealed that most of the samples had a density larger than 99.8%, Table 2, which agrees well with the trend of relative density estimated using the Archimedes method (Fig. 2). Based on these observations and combined with the density measurement results in Fig. 2, the suitable processing range of SLM could be determined to be the range of 300-370 W for the laser

power and 800 mm/s-1600 mm/s of the scan speed, as marked by the solid-line frame in Fig. 3.

To further confirm the structural integrity of the samples produced within the determined processing window, the non-destructive μ-CT technique has been used to display the 3D pore morphology and

Table 2
Relative density measured by analyses of images within the black-color solid-line frame in Fig. 3.

Laser power (W)	Scan speed (mm/s)			
	800	1000	1200	1600
370	99.67 ± 0.68	99.83 ± 0.16	99.92 ± 0.01	99.87 ± 0.03
350	99.91 ± 0.03	99.96 ± 0.01	99.91 ± 0.03	99.91 ± 0.02
300	99.93 ± 0.02	99.91 ± 0.05	99.93 ± 0.02	99.79 ± 0.06
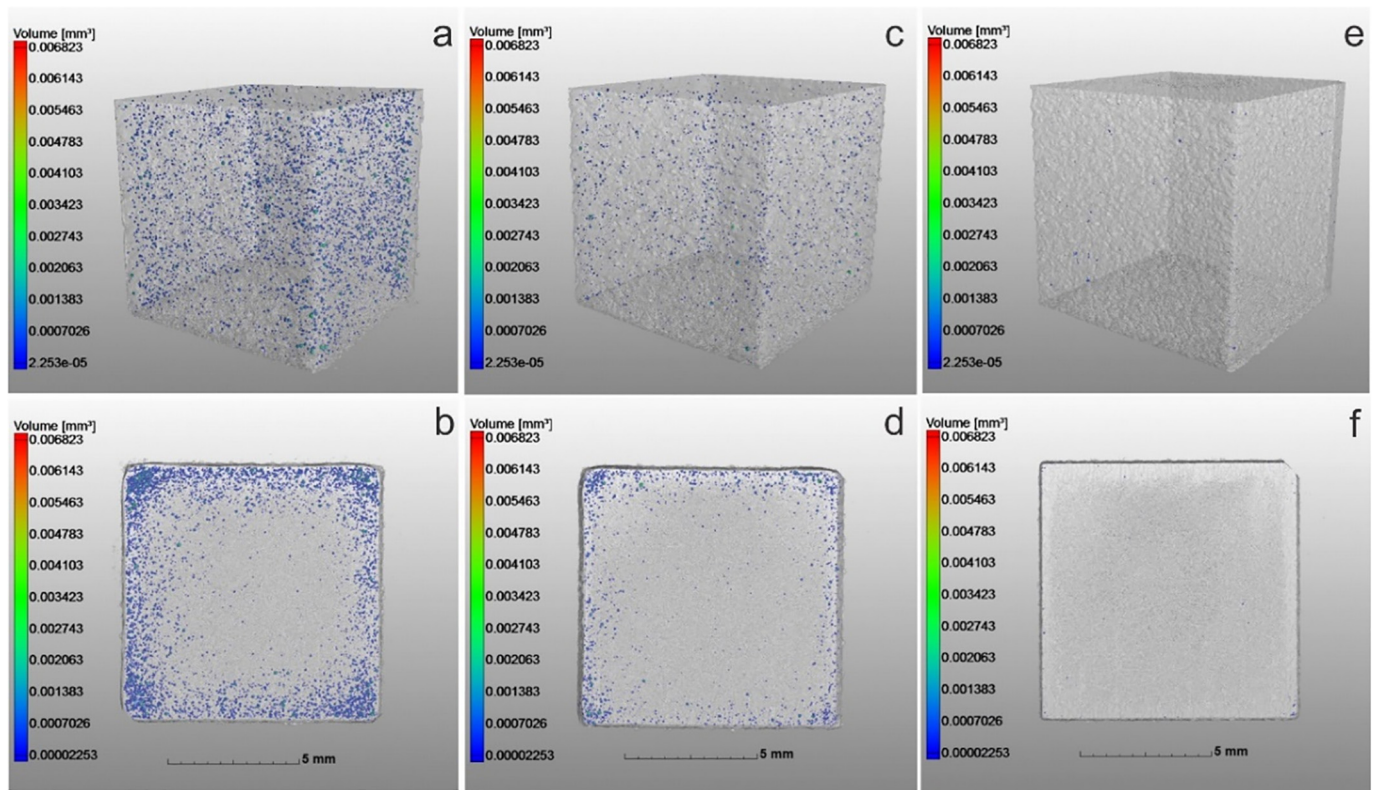
Fig. 4. Pores in as-fabricated sample cubes in 3D visualization (top) and observed along the XY projection (bottom) revealing the pore morphology and distribution reconstructed from the μ-CT images of (a–b) cube 1 (370 W, 1000 mm/s), (c–d) cube 2 (350 W, 1000 mm/s) and (e–f) cube 3 (350 W, 1600 mm/s).

distribution from three selected cubes (as outlined by the red-color dashed line in Fig. 3). The 3D representation of the pores from the μ-CT data displayed in Fig. 4, reveals no crack defects or sharp-edged pores existing in the three as-fabricated samples. However, it seems that the spatial distribution of the pores is not uniform, especially in cube 1 and cube 2. Also, cube 1 shown in Fig. 4(a) has the highest global porosity, where large amounts of regular pores are mainly clustered close to the surface and the edges. Compared with cube 1, a significant reduction in global porosity can be observed in cube 2 and cube 3, Fig. 4(d, f). The detailed porosity retrieved from μ-CT measurements is summarized in Table 3. Based on the table, as scan speed decreases from 1600 mm/s to 1000 mm/s, the global porosity increases from 8.6E-6% to 0.12%. However, the majority of the pores have mean sphericity $\Psi > 0.6$, which indicates that regular more than irregular pores dominates these cubes. No anisotropic pores were detected in any of the samples, opposite to the observations for AlSi10Mg [44].

The detailed pore size distribution in cubes 1, 2, and 3 is shown in Fig. 5(a). Here, the lognormal probability density function was chosen to fit the pore size distribution. Cube 1 produced with 370 W and 1000 mm/s has the highest number of pores (5955 pores, Table 3), where most of the pores have a size ranging from 40 to 120 μm with a

mean diameter size of 72.47 μm. Reducing the power to 350 W for cube 2 reduces the pore count (2085 pores) with the size ranging from 20 to 60 μm and a mean diameter of 32.88 μm. Increasing the scan speed to 1600 mm/s at a laser power of 350 W dramatically reduces the number of pores to 129. However, their mean diameter size increased to 57.65 μm with a size range of 40 to 80 μm.

Fig. 5(b) provides the sphericity of the pores as a function of the pore diameter. One can find most of the pores have their sphericity larger than 0.4. However, some minor irregular pores can still be seen, especially in cube 2 and 3, with the size ranging from 70 to 300 μm. Cube 3 shows the least number of pores with the majority having sphericity >0.4. Yet, some elongated pores with sphericity <0.4 exist too, and they are probably responsible for increasing the pore size range seen in Fig. 5(a). The irregular elongated pores are the geometrically characteristic of the lack of fusion pores.
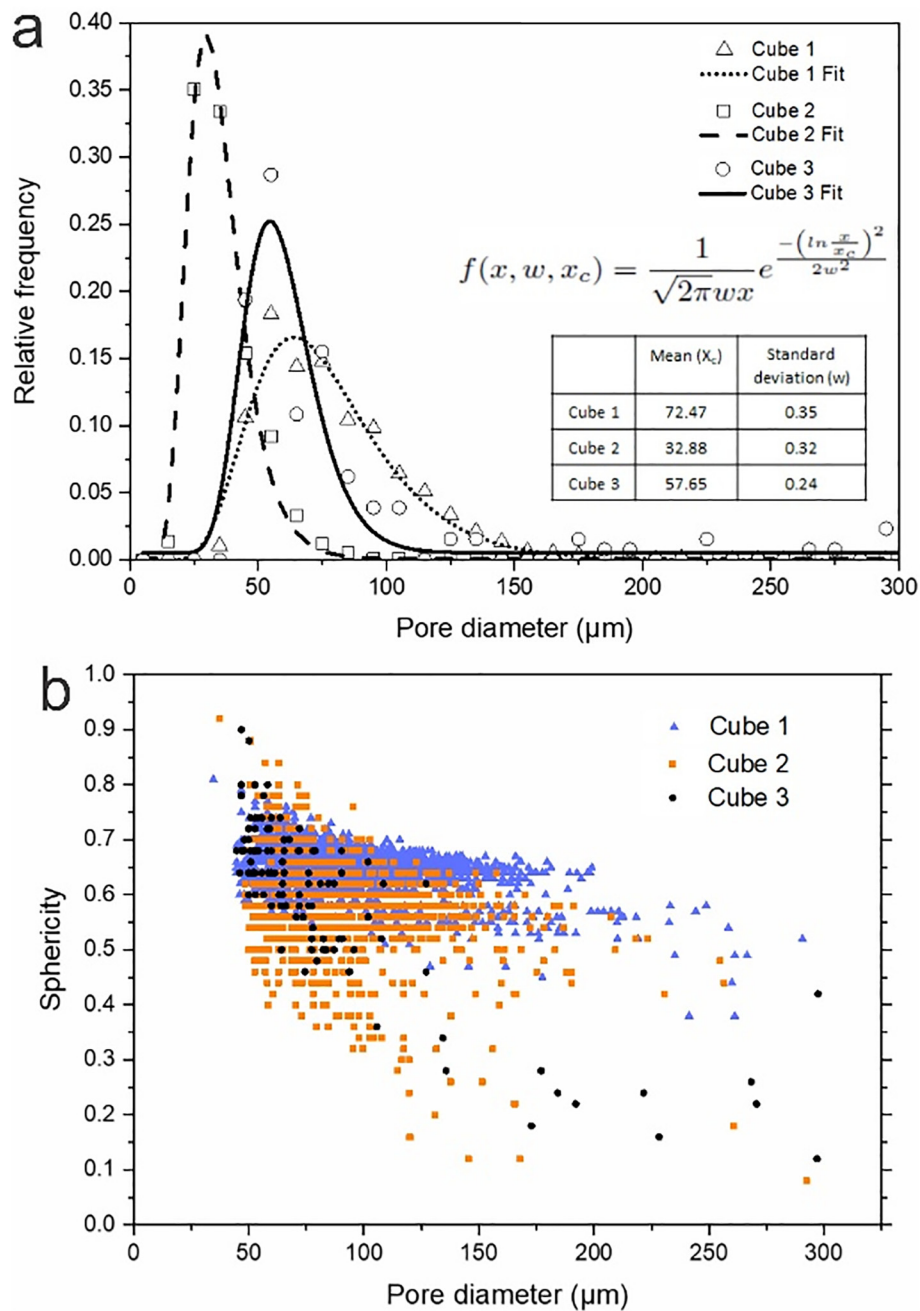
3.2. Mechanical properties

Three as-fabricated specimens processed within the optimized processing window were selected for tensile mechanical tests. Their tensile curves are provided in Fig. 6, for which their yield strength (YS), the ultimate tensile strength (UTS) and elongation are listed in Table 4. According to the tensile curves shown in Fig. 6, the difference in YS and UTS of these three samples is minimal, with slightly higher strength values for high scan speed (1600 mm/s) compared to low scan speed (1000 mm/s). They all achieve a yield strength >430 MPa with elongation >17.8%, Table 4. The slight reduction in ductility from 20% to 17.8% occurs upon reducing power from 350 W to 300 W with the same scan speed. Besides, the tensile curve shows a yield drop followed by a broad plateau of serrated yielding then the material flows till failure. A minimal work hardening can be observed from the minor difference between the YS and UTS.

Table 3
The μ-CT measurements showing the global porosity, relative density, total number of pores, and mean sphericity for the as-fabricated Al-Mn-Mg-Sc-Zr cubes.

Cube	Power (W)	Scan speed (mm/s)	Global porosity (vol%)	Relative density (%)	Total amount of pores	Mean sphericity Ψ
1	370	1000	0.12	99.88	5955	0.66
2	350	1000	0.03	99.97	2085	0.65
3	350	1600	8.6E-6	99.99	129	0.62

$$f(x, w, x_c) = \frac{1}{\sqrt{2\pi}wx} e^{\frac{-\left(ln\frac{x}{x_c}\right)^2}{2w^2}}$$

	Mean (X_c)	Standard deviation (w)
Cube 1	72.47	0.35
Cube 2	32.88	0.32
Cube 3	57.65	0.24

Fig. 5. Pore analysis retrieved from μ-CT measurements for three cubes showing (a) pore size distribution with lognormal distribution fitting, and (b) sphericity as a function of pore diameter.

3.3. Microstructure characteristics

The general microstructure examination for the as-fabricated samples reveals the typical bimodal structure associated with the alloy, such as those shown in Fig. 7. The layer-wise features along the build direction reveal good bonding without apparent interlayer cracking, Fig. 7(a). A closer inspection of a single melt pool in Fig. 7(b) reveals the dark and bright contrasts denoting different morphological responses to the chemical etchant. The melt pool, marked with the red dotted line, consists of a bright core with a darker area extending towards the boundary. The SEM imaging was performed to analyze further the difference of the microstructural features between the bright and dark areas. As shown in Fig. 7(c), the center area of the melt pool, that appears brighter in Fig. 7(b), corresponds to columnar and relatively coarse grain (CG) region, while the bottom darker area of the melt pool consists of fine

grains (FG). A higher magnification for melt pool boundary, displayed in Fig. 7(d), shows the distinct transition from CG to FG, indicating that both regions experience different modes of solidification.

The CG region consists of elongated columnar grains with an average grain width of 2.4 ± 1.7 μm clustering in bands with thickness around 20–70 μm, Fig. 8(a-b). Due to the large thermal gradient that exists across the melt pool, CG grows preferably along the build direction, as shown by the corresponding pole figure, Fig. 8(c). In comparison, the high-magnification EBSD image of an FG region in Fig. 8(b) reveals a sub-micron equiaxed morphology with less preferable orientation, as shown by the relatively weak texture of the corresponding pole figure in Fig. 8(d).

The bimodal microstructure was further examined by STEM imaging, as shown in Fig. 9. Inspection of Fig. 9(a) reveals CG and FG regions existing in the top and bottom parts of the image, respectively. Also,
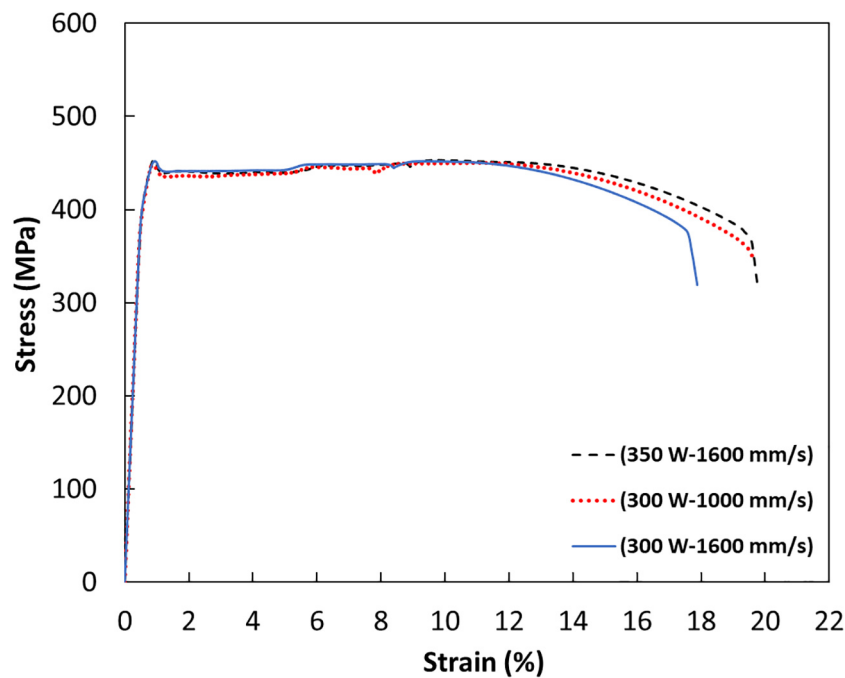
Fig. 6. Engineering stress-strain curves for three selected samples (300 W, 1000 mm/s; 300 W, 1600 mm/s; 350 W, 1600 mm/s) in the optimized processing window in Fig. 3.

there is a high number density of intermetallic particles existing inside the grains and along the boundaries of both CGs and FGs. Most particles along grain boundaries have a size range from 100 nm to 200 nm. Also, they are all brighter than the matrix in the HAADFSTEM image shown in Fig. 9(b).

By using relatively high-magnification STEM imaging for the FG region, Fig. 10(a–b), it has been revealed that the particles along the grain boundaries, though appear interconnected in Fig. 9, actually consist of more than one phase. The corresponding element distribution for Fig. 10(a–b), shown by STEM-EDS maps in Fig. 10(c–h), reveals two types of phases existing in the FG region. One of the phases, enriched in Sc and distributes inside the grains and along the grain boundaries. These Sc-rich particles exist inside grains (marked by dashed-line circles) have a cube-shape with a typical size range of 20–50 nm, which is smaller than those along grain boundaries. The other phase mainly distributes along grain boundaries and is enriched in Mn. This can be further confirmed by Fig. 10(g), where Mn-rich and Sc-rich particles at the grain boundaries are not superimposing. Besides, part regions of Mn-rich particles contain Fe concentration, Fig. 10(h). Fig. 11 provides STEM-EDS maps for a CG region. Similar to FG, the Mn (Fe)-rich particles are observed along the grain boundaries, Fig. 11(g). Unlike FG, however, fewer Sc-rich particles exist in the CG.

One of the cube-shaped Sc-rich particles inside FG grains, i.e. those shown by dashed-line circles in Fig. 10(a), is selected for further study from the atomic scale. As shown by the HAADF-STEM image in Fig. 12 (a), the Sc-rich particle has a width of ~30 nm in this viewing direction. From the enlarged image of a local region of the particle, many regularly-arranged bright dots can be observed. Each bright dot

represents a column rich in Sc atoms because the brightness of individual atomic columns in HAADF-STEM images approximates the square of the averaged atomic number (the atom number is 13 for Al and 21 for Sc). Furthermore, these Sc-rich atomic columns have a regular separation distance of ~0.41 nm along the horizontal direction, based on the measurement that was made from the calibrated image. According to these characteristic features, the Sc-rich phase was confirmed to be the Al_3Sc that has the $L1_2$ structure with a lattice parameter of $a = 0.4103$ nm, Fig. 12(c). The distribution of the Sc and Al columns inside the unit cell, as indicated by the blue dashed-line frame in Fig. 12(b), is consistent with the Al_3Sc structure projected along the <110> direction, Fig. 12(d).

Having identified the Sc-rich phase of Al_3Sc in FG, we further examined the Mn-rich phase in CG. Fig. 12(e) provides a typical HAADF-STEM image showing a Mn(Fe)-rich particle existing in the CG grain in Fig. 11 (a). Such a particle has a relatively round shape with a dimension of ~50 nm and brighter contrast than the matrix (atomic number is 25 for Mn and 26 for Fe). The structure of the particle was further examined by atomic-scale HAADF-STEM imaging, Fig. 12(f). From the image and corresponding Fourier-filtered image inserted, a ten-fold symmetry can be revealed, indicating a quasicrystal structure.

4. Discussion

The current work has shown that the Al-Mn-Mg-Sc-Zr alloy is well processable with SLM within the established processing window, where the built samples can achieve materials density more than 99.8%, without solidification cracking or major metallurgical defects. Also, the processing window is robust and industrially favorable. Besides, the excellent mechanical properties of the built samples exhibit a low sensitivity to laser parameter variation. Solid solution strengthening, exceptional refinement, along with two different types of intermetallic particles, endow the alloy a superior mechanical performance.

4.1. Optimum processing window

The optimum processing window, containing laser power in the range of 300–370 W and scan speed in the range of 800–1600 mm/s,

Table 4
Values of yield strength (YS), ultimate tensile strength (UTS) and elongation from the curves shown in Fig. 6.

Processing parameters	300 W, 1000 mm/s	300 W, 1600 mm/s	350 W, 1600 mm/s
0.2% YS (MPa)	430.7 ± 4.5	435.3 ± 1.2	438 ± 3.8
UTS (MPa)	446.9 ± 3.9	451.7 ± 0.4	451.8 ± 2.2
Elongation %	19.4 ± 0.6	17.8 ± 0.5	20 ± 1.2
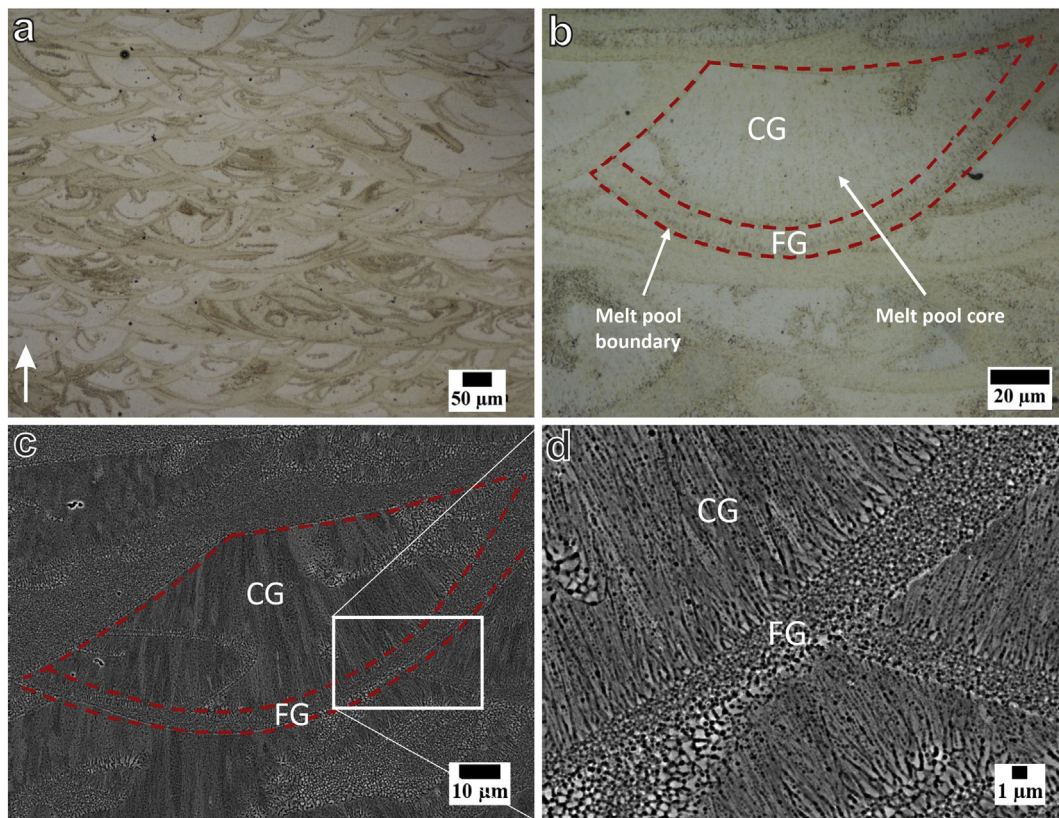
Fig. 7. OM image of (a) an as-fabricated sample processed with (300 W, 1600 mm/s) in low magnification, (inserted white arrow represents building direction), (b) high magnification of a single melt pool, SEM BSE image of (c) high magnification of a single melt pool, (d) high magnification of the area marked with the white rectangle in (c).

has been established in this work. Within the determined processing window, all the samples have a relative density higher than 99.8%. Porosity analysis has revealed a high consolidation region with no significant metallurgical defects. The lower laser power beyond the current established range, i.e., < 300 W, will lead to an insufficient energy penetration in the powder. Then the insufficient energy input will give rise to disordered solidification front, where the powder experiences low wettability. Hence the liquid phase is insufficient to fill up the cracks [1,45]. Thus, relatively high energy input is needed to account for the rapid heat dissipation that takes place through the solidified material typically due to the high thermal conductivity and high reflectivity of Al [38]. Increasing the laser power to 300 W and above in this work can improve the wettability of the powder and the flowability of the melt pool by reducing the dynamic viscosity of the Al alloy liquid [29]. Therefore, the pores are easily filled with the liquid phase, and the densification is enhanced, leading to optimum fusion. Yet increasing the laser scan speed to 2000 mm/s apparently reduces the laser energy input on the processed powder layer, which induces the gradual recurrence of irregular lack of fusion pores. Though using faster scan speeds is a means for increasing the fabrication efficiency, reaching 2000 mm/s is obviously too fast to achieve complete powder melting, which leads to poor powder wettability.

On the other hand, applying excessive energy input (the scan speed less than 800 mm/s and laser power higher than 300 W) intensifies the effect of thermal conductivity [46] and disturbs the melt pool due to slow cooling, which will give rise to large evaporation pores. This is mainly attributed to the severe Marangoni flow that arises from the extended interaction time between the laser and the metal powder at low scan speed and high power [28]. Furthermore, the laser beam induces evaporation for part of the molten material when it conveys high energy input to the powder. Consequently, the alloying elements might be depleted, which will not only affect the solid solution and precipitation strengthening but also decreases the stability of the scanning tracks [47]. Especially, elements with low vaporization temperature, such as Mg, will generate high recoil pressure [1,29]. As a result, round pores filled with vapors or gases tend to form at the end of laser scan tracks [1] and get entrapped in the melt pool due to the nonequilibrium convection flow associated with extra high energy input.

For those samples built within the optimum processing window, the μ-CT has been used in this work to get more insight into the relationship between the processing parameters and the porosity distribution and evolution. The results have provided a fair evidence that the laser energy input used to produce the investigated cubes was sufficient to achieve thorough melting for the metal powder, which was reflected in high consolidation with a global level of porosity <0.15% in all cubes. Besides, there is no major lack-of-fusion cracks, only regular (relatively round) pores prevail in all the cubes, which mostly form due to vaporization and gas entrapment during SLM. Typical smaller gas pores (< 5 μm) are expected to form too [48]. However, they are expectedly below the detection limit of the μ-CT since the threshold of the software was set to eight voxels. Therefore, the global porosity might be underestimated, leading to the excellent consolidation reflected in cube 3 (~99.99%), as displayed in Fig. 4(c). Yet these gas pores are not expected to significantly increase the global porosity. The porosity analyses by μ-CT have also provided further evidence that the laser parameters and hence energy input do affect the number, size, morphology, and distribution of the pores. Especially, the pores that are not distributed uniformly inside the sample cube have been observed. Many of them appeared close to the surface or edges of the samples. This can be explained by the lower solidification rate of the melt pool at the edges compared to the central area due to the adjacency of these edges to the feedstock powder. The existence of air-filled gaps in the surrounding powders and the smaller contact area among powder particles, tend to reduce the thermal conductivity of the powder compared
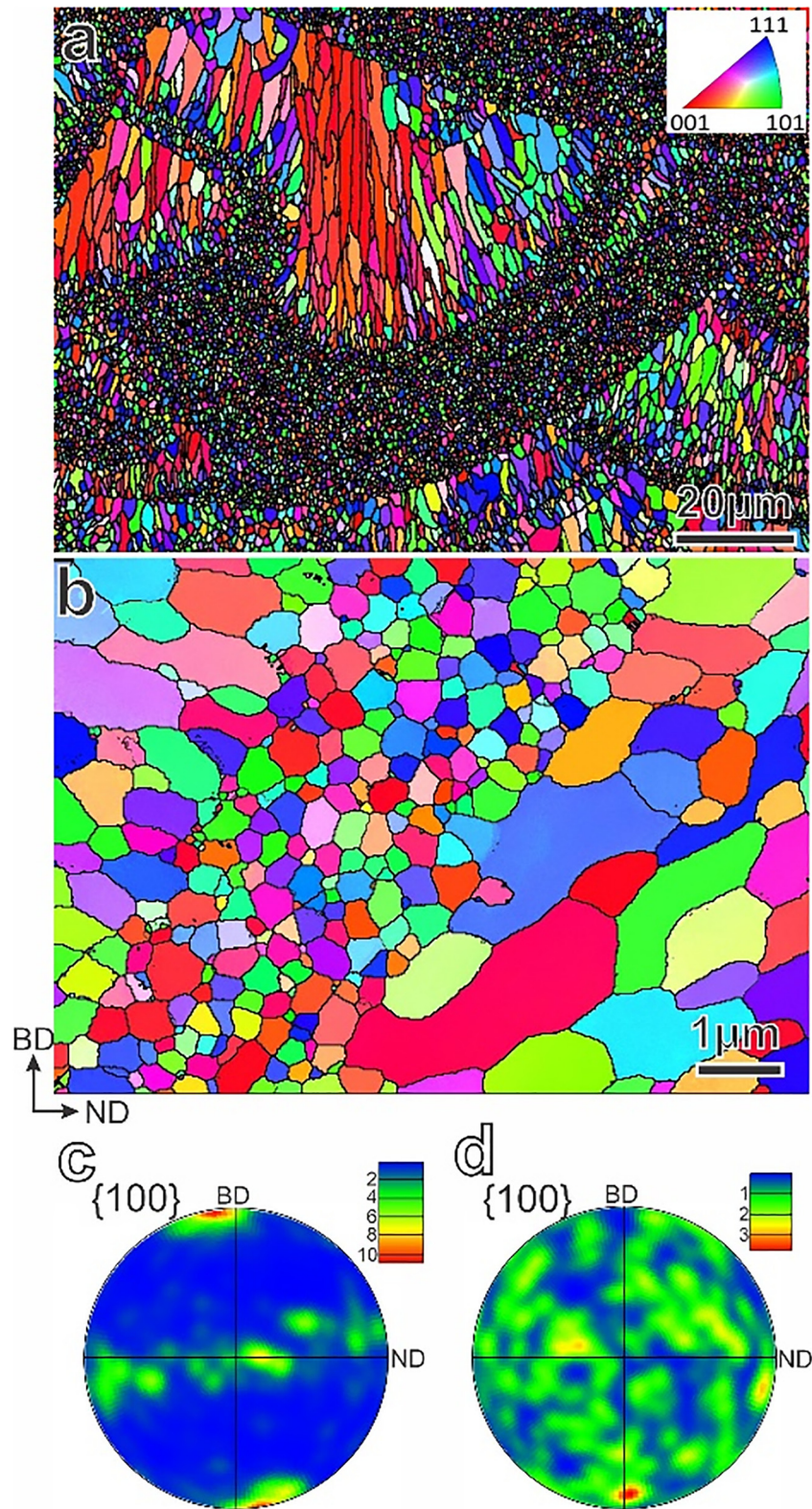
Fig. 8. EBSD inverse pole figure (IPF) map of an as-fabricated sample processed with (300 W, 1600 mm/s) showing (a) alternating layers of FG and CG that form along the building direction, (b) high magnification EBSD displaying the submicron equiaxed grains in an FG area, the IPF maps displayed in (a) and (b) were generated by choosing the building direction (BD) as the projection axis, ND is the direction normal to the building direction, (c-d) corresponding pole figures from CG region and FG region respectively.

with the bulk material in the center [49]. Therefore, powders surrounding the edges insulate the building part and reduce the heat dissipation from the edges to the surrounding metal powders compared with the bulk material in the center.

To reflect the combined effects of laser power and scan speed on the density of the material and compared with the previous work, we further consider volumetric laser energy input here. The volumetric laser energy input, E_v, is expressed as [13].
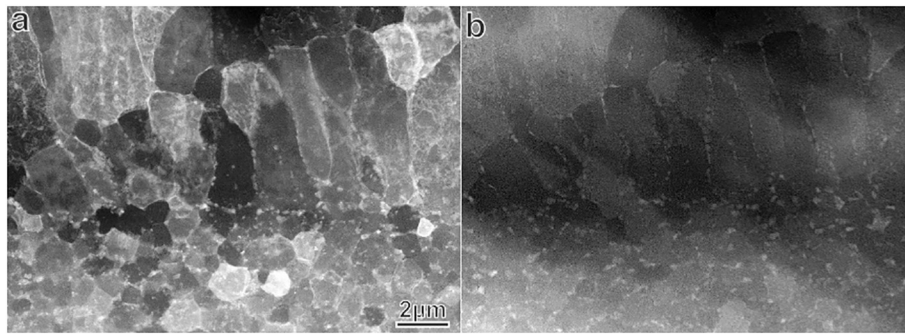
Fig. 9. (a) LAADF-STEM of as-fabricated sample processed with (300 W, 1600 mm/s) showing CG and FG regions, (b) corresponding HAADF-STEM image showing the high number density of bright particles existing in both CG and FG regions.

$$E_v = \frac{P}{V.h.t} \qquad (2)$$

where P is laser power (W), V is scan speed (mm/s), h is hatch distance (mm), t is powder layer thickness (mm).

According to the equation, the energy density of the investigated processing parameters was calculated and shown in Fig. 13. The determined processing window lies within the E_v range of 60–160 J/mm³. A sharp drop in material density takes place as the energy input goes below 60 J/mm³. Further density reduction is observed at E_v higher than 160 J/mm³. When E_v values are between 60 J/mm³ and 160 J/mm³, the relative density becomes steady. Based on Table 3, reducing the energy density from 123.33 J/mm³ to 116.67 J/mm³ by decreasing the power by only 20 W to 350 W, while keeping the same scan speed of 1000 mm/s, reduces the pores count to more than half and cut down mean size by ~55%. However, the majority of the pores are clustering close to the edges. They have the similar regular morphology to the evaporation pores, which implies that an E_v of 116.67 J/mm³ is still marginally high. With further reducing the energy to 72.92 J/mm³ by increasing the scan speed to 1600 mm/s at the same power 350 W, the global porosity significantly reduced to <0.01%. Nevertheless,

minor irregular pores started to form with the size beyond 70 µm, as can be observed from Fig. 5(b). Therefore, we suggest not to increase E_v beyond ~110 J/mm³ to minimize the global porosity in the SLM parts. Although good attainable material density > 99.8% can be achieved in a range of E_v between 60 and 160 J/mm3. The porosity analysis retrieved from µCT of cube samples allows rendering the processing window between 70 and 110 J/mm³. This window can achieve very low global porosity (< 0.05%). This result is in line with the work reported by Shi et al. [27] in which an E_v range of 77–103 J/mm³ has been suggested for a good compromise between porosity and solute supersaturation for a hypereutectic Sc (1.08 wt%) content. However, the processing window suggested here is lower than the optimum energy input value suggested by Spierings et al. [34], who recommended an optimal range of E_v of 125–150 J/mm³ for the Scalmalloy.

4.2. Excellent mechanical properties

The tensile testing results in this work have shown excellent mechanical properties with low deviation within the established processing window. The yield strength of the alloy in the as-fabricated condition can reach 430 MPa with the elongation of 17%. These values
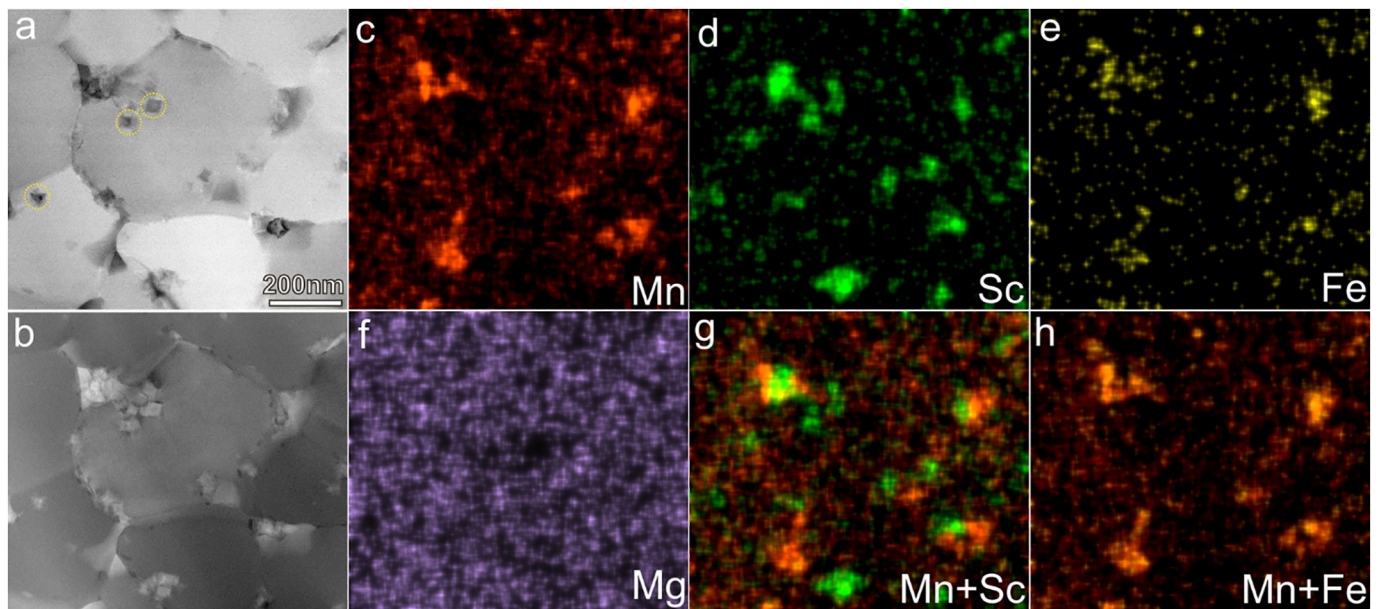
Fig. 10. (a) BF-STEM and (b) HAADF-STEM images for the FG region of as-fabricated sample (processed with 300 W and 1600 mm/s) showing different particles existing in the microstructure, and (c-h) corresponding STEM-EDS maps showing the composition of these particles existing in the FG region. By overlaying Mn (red) and Sc (green) in (g), and Mn (red) and Fe (yellow) in (h), two types of particles are confirmed, and they are enriched in Sc and Mn(Fe), respectively.
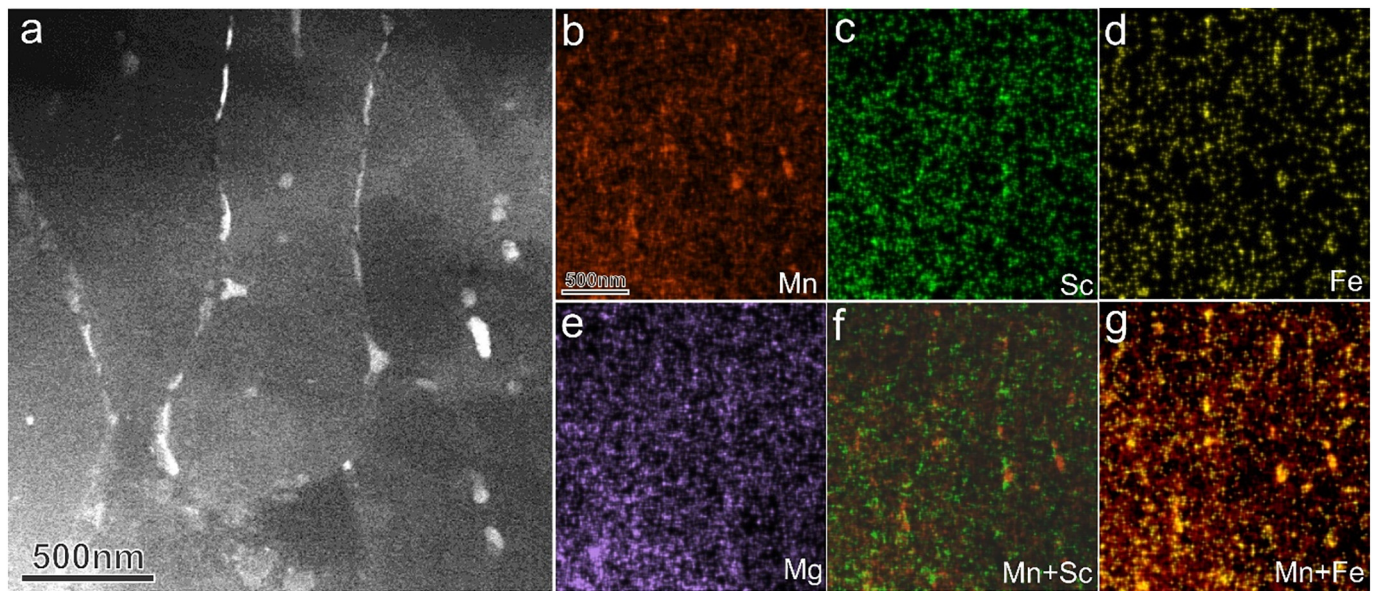
Fig. 11. (a) LAADF-STEM image for a CG region of the as-fabricated sample (processed with 300 W and 1600 mm/s) showing the smaller number of particles compared with the FG region, and (b-g) corresponding STEM-EDS maps showing the composition of these particles. By overlay of Mn (red) and Sc (green) in (f), Mn (red), and Fe (yellow) in (g), both Sc-rich and Mn (Fe)-rich particles are confirmed.

are significantly higher than those of Al—Si alloys produced by SLM (Typical yield strength below 300 MPa whether in as-fabricated or heat-treated conditions) [1,2,5]. Compared with the values reported for hypereutectic Al—Sc alloys, the as-fabricated yield strength reported in this work is still superior. Spierings et al. [31,33] reported for Scalmalloy a yield strength in the range of 270–310 MPa for as-fabricated condition. The yield strength of the as-fabricated Al-3.4 Mg-1.08Sc-0.23Zr-0.5Mn-0.44Cu alloy was reported to be in a range of 250–380 MPa with limited ductility less than 6 % [50]. Our alloy exhibited higher strength compared with Al—Cu alloys processed by SLM [15], reporting a yield strength of around 276 MPa with a ductility of around 6%. In addition, the yield strength of our alloy exceeded that of wrought 2024-T6 [51] and as-cast Al-5 Mg-0.6Sc alloy [52].

4.3. Characteristic microstructure

The characteristic microstructure associated with the excellent mechanical properties of the alloys has been revealed in this work. Such microstructure contains two distinct grain regions: a coarse grain region constituting the melt pool core and a fine grain region locating around the melt pool boundaries. A similar bimodal microstructure has been reported in other Sc-containing Al alloys processed by SLM [32,53]. Our work also showed that the ratio of the FG region to CG could be affected by the laser energy input, as shown in Fig. 14(c). As E_v decreases, CG regions tend to extend at the expense of FG regions. Previous work has suggested that such ratio change is controlled by the ratio of the thermal gradient (G) and growth rate (R) [53]. Columnar grain formation is usually stimulated by high G and low R. Low E_v levels (low power and high scan speed) increase G/R ratio and promote columnar grain formation [38]. Therefore, in this work, the area fraction of FG decreases from around 53% to 41% with decreasing E_v. This reduction seems not to apparently affect the tensile yield strength of the alloy (Fig. 6).

It has been previously suggested that Sc additions have potent effects on enhancing the mechanical properties of Al alloys [22–24]. The cube-shaped Sc-rich intragranular particles have been identified as Al₃Sc, as shown in Fig. 12(b-c). Hypereutectic Al—Sc (~0.6 wt% Sc), form upon solidification primary Al₃Sc particles with the L1₂ structure. These Al₃Sc particles act effectively as heterogeneous nucleation sites for the solidification of α-Al grains [22]. To account for the possibility that the eutectic composition might shift to the right due to the ultrafast

cooling rates in SLM, the Sc content in our alloy (0.91 wt%) was kept higher than the eutectic composition. Consequently, many primary Al₃Sc particles form in the melt [22]. After solidification, the remnant heat caused by next laser scans can further promote the growth of the primary Al₃Sc particles. At the size range of 20–50 nm for Al₃Sc particles, they were suggested to be semi-coherent with the matrix in a previous work [54]. It worth noting that not all of the primary Al₃Sc particles appearing within the equiaxed grains in Fig. 10(a–b) are necessarily acting as seed crystals for the α-Al matrix [55]. The extra intragranular Al₃Sc particles can though have a little contribution to the strength. In addition to acting as seed crystals, Al₃Sc particles are also seen at the grain boundaries where they might be pushed ahead of the solidification front [56]. Besides, some of these particles may have precipitated at the grain boundaries stimulated by the cycling heat treatment during the laser scanning in the next layers.

The resultant fine grain morphology would be capable of accommodating the localised strains resulting from the rapid cooling, and in turn mitigating hot tearing in comparison to the non-weldable and crack-sensitive Al alloys of the 2000 and 7000 series [21]. In addition, the large area fraction of fine equiaxed grains with no preferential orientation provides the resistance to dislocation motion, thereby the high strength [57]. It should be noted that the temperature difference throughout the melt pool can induce a non-uniform density distribution of the Al₃Sc primary particles [32]. We propose that the equiaxed FG bands displayed in Fig. 7 form aided by the Al₃Sc primary particles that nucleate at the cooler remelting zones that lie at the melt pool boundary. On the other hand, at higher temperature areas towards the center and top parts of the melt pool, where Al₃Sc seed crystals dissolve, columnar grains form. Despite many primary Al₃Sc particles existing in the as-fabricated microstructure, an atom probe tomography (APT) analysis, for a similar alloy system, confirmed that there are still abundant supersaturated Sc in the Al matrix [36]. The supersaturation of Sc in the Al matrix can also contribute to the strength of the material by solid solution strengthening [58]. Besides, they are available to precipitate secondary Al₃Sc upon further heat treatments [36].

Among different alloying elements, Mn confers important improvements to Al alloy properties, including excellent workability, weldability, and corrosion resistance [51]. Additionally, it has been established that Mn is effective in strengthening Al alloys, as long as Mn is in solid solution [59]. This is because Mn solubility in Al can be
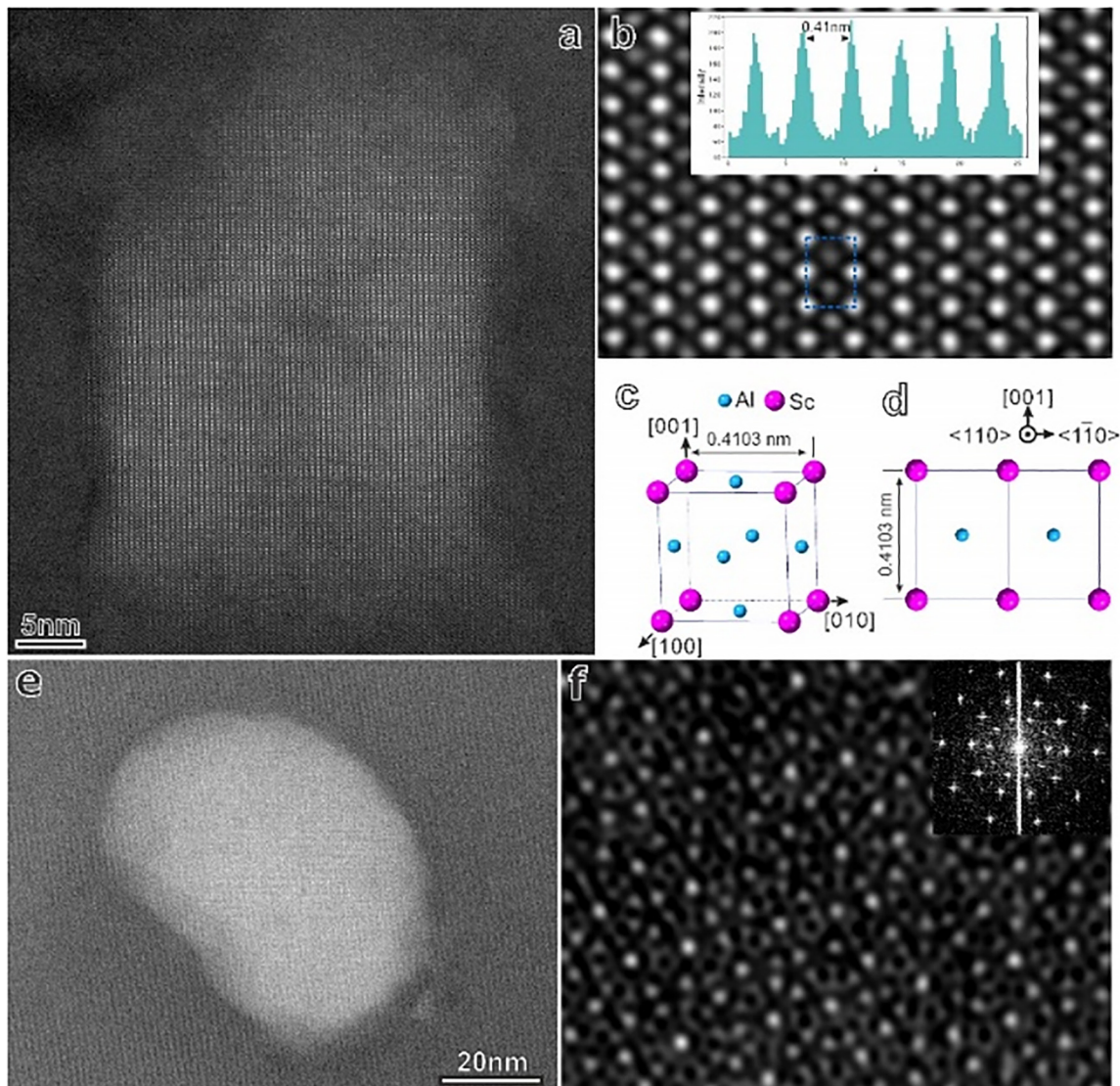
Fig. 12. (a) Atomic-scale HAADF-STEM image displaying a typical cube-shaped Sc-rich intragranular particle from FG region, (b) enlarged image from (a) confirms this particle is Al_3Sc ($L1_2$, $a = 0.4103$ nm) viewed along $\langle 110 \rangle$ direction, (c-d) schematic diagram showing the unit cell of the Al_3Sc, and its projection along <110>, (e) HAADF-STEM image displaying a typical round-shaped Mn(Fe)-rich particle from CG region, and (f) corresponding atomic-scale HAADF-STEM image showing the quasicrystal structure with a ten-fold symmetry, as shown by the inserted Fourier-filtered image.

further extended by rapid solidification, which is an advantage of SLM [60]. The ultrafast cooling rates in SLM processing can retain up to 4.3 wt% of Mn in supersaturated solid solution, which greatly exceeds its equilibrium solubility (~1.8 wt%) [36]. The solid solution strengthening effect of Mn can exceed that of Mg in commercial Al alloys [61]. Specifically, every 1 wt% of Mn in solid solution can enhance the yield strength by 30.3 MPa [59]. Note that the Mg content was deliberately controlled in our alloy to below 1.5 wt% in order to avoid the evaporation and oxidation susceptivity of Mg during SLM processing [5]. The vaporization temperature of Mg (~1110 °C) is half that of Mn (~2150 °C). Thus, high Mg content can trigger processing instabilities due to evaporation, provided that the melt pool temperature can reach up to 2500 °C [32]. Therefore, higher content of Mn relative to Mg can further increase the strength by solid solution strengthening and can ensure a greater degree of stability. This supports the remarkably improved tensile properties of our AlMnScZr system compared to AlMgScZr system. An early work on Mn-containing Al alloys has revealed Mn-rich particles along the grain and subgrain boundaries [60], which is consistent with our observations in both FG and CG regions. It seems that as the melt pool cools down, Mn is pushed ahead of the advancing solidification front preferentially aggregating at the grain boundaries. During the layer by layer SLM building process, the absorbed heat from the laser energy will be mainly dissipated through the solidified layers. The cyclic reheating will then in-situ heat-treat the previously consolidated material. During this intrinsic heat treatment, the grain boundaries may act as the diffusional pathway, through which Mn-rich intermetallic can further form and grow. These Mn-rich particles have been previously suggested to pin grain boundaries and retard grain growth during processing [51,59]. It should also be emphasized that the EDS maps for FG and CG displayed in Fig. 10(f) and Fig. 11(f) show that Mn and Sc are enriched in two different types of particles. This means that mostly Mn does not interact with Sc to form non-hardening Mn—Sc phases. Hence, Mn should not reduce the solubility of Sc supersaturated in solid solution.

The HAADF-STEM study in Fig. 12(f) has confirmed a Mn(Fe)-rich quasicrystal structure in the as-fabricated material. These nanoscale quasicrystals are mainly distributed within CG grains. Previous studies [62,63] have reported the formation of quasicrystal or quasicrystal approximant in rapidly-solidified Al—Mn alloys. In addition, some Fe concentration has been detected in these Mn-rich quasicrystal particles.
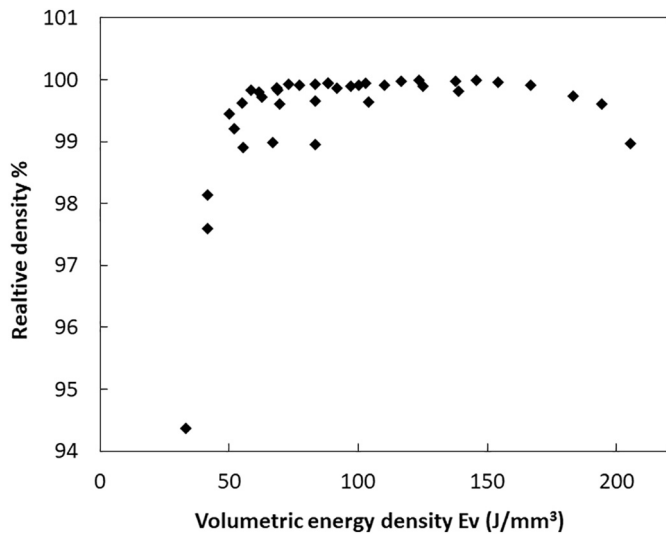
Fig. 13. The dependence of material density on volumetric energy density (E_v).

cooling rates acting as a quenching effect to the melt pool will lead to the non-equilibrium microstructure including the quasicrystal structure [38]. Yet, the quenching effect apparently cannot provide enough time for the crystallization of the metastable structure after its formation. It has been reported that the dispersed Mn(Fe)-rich particles can assist in promoting grain refinement [59,66]. Furthermore, the formation of non-periodic, quasicrystal phases has been identified as a promising strategy for reinforcing Al alloys [63,67,68]. Thus, a dispersion of nano-size quasicrystal particles in the microstructure is expected to contribute to the high strength of the Al alloys by particle strengthening [67].

Based on above discussion, the grain refinement effect of both Sc and Mn, in addition to the stability that Mn confer to the melt pool during processing further, has broadened the processing window of Al-Sc-Zr alloy system designed for SLM. Furthermore, it has led to the repeatability of an outstanding mechanical performance at different levels of processing energy density. The strengthening mechanisms that contribute to the outstanding mechanical properties of the as-fabricated material in this work have been assigned to the unique microstructural features, including bimodal grain structures, large area fraction of fine submicron grains, supersaturation of solutes in solid solution, and grain boundaries pinning particles. It should be noted that the high number density of Sc-rich and Mn(Fe)-rich particles can effectively pin the grain boundaries, especially in FG region, and thus can strengthen the material. This can be evidenced by the grain size comparison shown in Fig. 14(d), where the grain sizes at different E_v levels are quite similar and less than 600 nm. Apart from the high strength, the alloy also has a decent ductility, which is believed to be the results of the coarse grains that have a better capacity to accommodate tensile deformation [57]. Therefore, the columnar-equiaxed bimodal grain structure contributes to a good combination of strength and ductility [69].
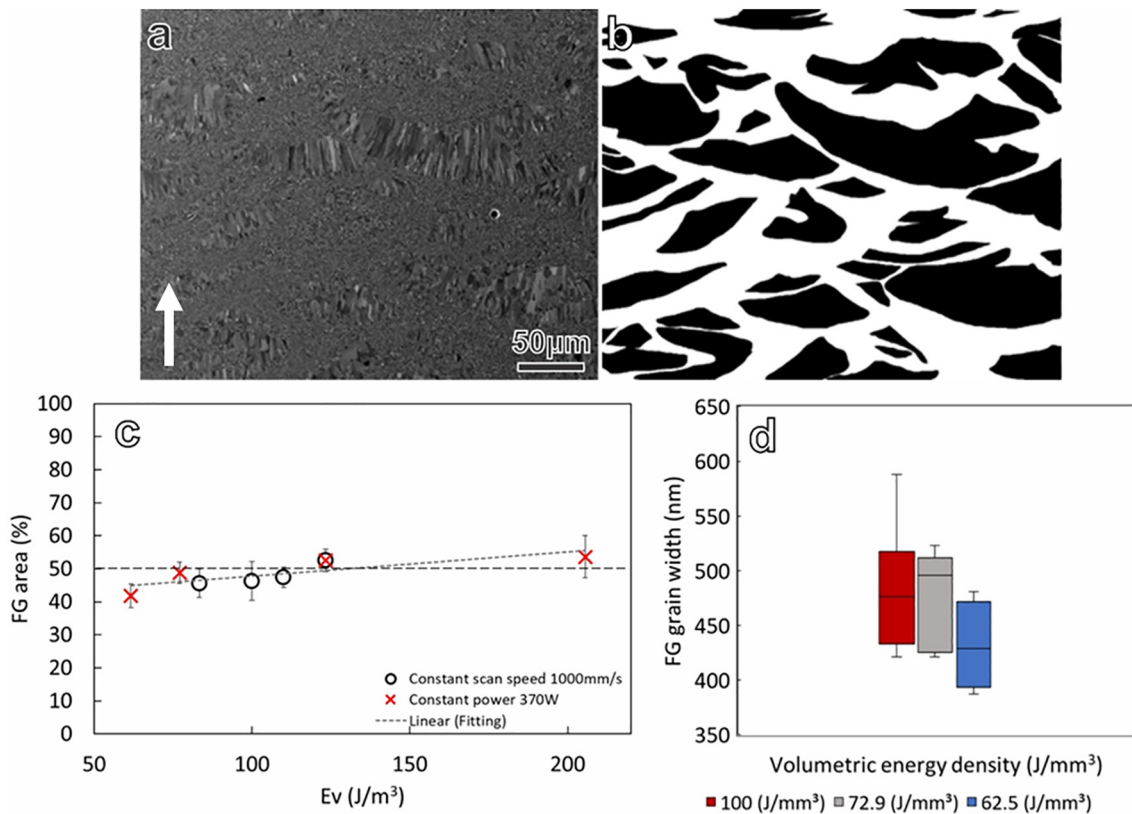
Such Fe may play a role in the stabilization of the quasicrystal phase in the alloy, which has been suggested by previous studies [63–65]. In SLM processing, a highly localised heat source (laser spot size of around 100 μm) is used for melting Al powder. Partial laser absorption by the Al powder takes place [5], then most of the heat absorbed by the melt pool will be dissipated through the consolidated surrounding material. Taking into account the high thermal conductivity of Al, the melt pool will experience the ultrafast cooling rates in the order of 10^5–10^6 K/s [34]. The high

Fig. 14. A typical SEM-BSE image from a sample processed with the parameters of 370 W and 1000 mm/s for the analysis of FG area fraction (inserted white arrow is the building direction), (b) processed image of (a) using ImageJ by segmenting the CG regions with masks, (c) the FG area fraction (%) in different E_v, (d) box plot showing the variation of FG grain width at different E_v.

5. Conclusions

In summary, the processing parameters for SLM production of a novel Al-Mn-Mg-Sc-Zr alloy were systematically explored, and the optimum processing range has been established. Also, the influence of processing parameters on the densification, mechanical properties, and microstructure were investigated. The following conclusions can be made:

1. The Al-Mn-Mg-Sc-Zr alloy is processable with SLM with a wide processing window. The window covers the laser power in the range of 300-370 W and scan speeds between 800 and 1600 mm/s, associated with the optimum laser energy density range of 70–110 J/mm^3.
2. The relative density of materials produced within such a window are all above 99.8%. The majority of the detected pores using the established processing parameters are relatively round with regular geometry. There are no cracks and lack-of-fusion pores.
3. The mechanical properties of as-fabricated samples show an excellent combination of strength and ductility that have low sensitivity to laser parameter variation. The alloy has a yield strength exceeding 430 MPa with more than 17.8% elongation at different laser parameters.
4. The microstructure of the as-fabricated material involves a unique bimodal grain structure. Fine equiaxed grain region with no preferential crystallographic orientation constitute the melt pool boundary, while coarser columnar grains prevail in the melt pool core preferentially growing along the building direction.
5. Two types of intermetallic particles have been observed in both coarse and fine grain areas. They are confirmed to be Al$_3$Sc and Mn (Fe)-rich quasicrystal phases. They are expected to pin the grain boundaries and stabilizes the microstructure by preventing grain growth at different laser energy levels.

Declaration of Competing Interest

The authors declare that they have no known competing financial interests or personal relationships that could have appeared to influence the work reported in this paper.

References

[1] L. Bian, N. Shamsaei, J.M. Usher, Laser-Based Additive Manufacturing of Metal Parts: Modeling, Optimization, and Control of Mechanical Properties, first ed. CRC press, London, NewYork, 2017.

[2] S. Lathabai, Additive manufacturing of aluminium-based alloys and composites, in: R.N. Lumley (Ed.), Fundamentals of Aluminium Metallurgy: Recent Advances, Elsevier 2018, pp. 47–92.

[3] P. Rometsch, Q. Jia, K.V. Yang, X. Wu, Aluminum alloys for selective laser melting – towards improved performance, in: F. Froes, R. Boyer (Eds.), Additive Manufacturing for the Aerospace Industry, Elsevier 2019, pp. 301–325.

[4] T. DebRoy, H.L. Wei, J.S. Zuback, T. Mukherjee, J.W. Elmer, J.O. Milewski, A.M. Beese, A. Wilson-Heid, A. De, W. Zhang, Additive manufacturing of metallic components – process, structure and properties, Prog. Mater. Sci. 92 (2018) 112–224.

[5] N.T. Aboulkhair, M. Simonelli, L. Parry, I. Ashcroft, C. Tuck, R. Hague, 3D printing of Aluminium alloys: additive manufacturing of Aluminium alloys using selective laser melting, Prog. Mater. Sci. 106 (2019) 100578.

[6] S.Q. Wu, Y.J. Lu, Y.L. Gan, T.T. Huang, C.Q. Zhao, J.J. Lin, S. Guo, J.X. Lin, Microstructural evolution and microhardness of a selective-laser- melted Ti-6Al-4V alloy after post heat treatments, J. Alloys Compd. 672 (2016) 643–652.

[7] M.S.F. De Lima, S. Sankaré, Microstructure and mechanical behavior of laser additive manufactured AISI 316 stainless steel stringers, Mater. Des. 55 (2014) 526–532.

[8] M. Sadowski, L. Ladani, W. Brindley, J. Romano, Optimizing quality of additively manufactured Inconel 718 using powder bed laser melting process, Addit. Manuf. 11 (2016) 60–70.

[9] A. Takaichi, T. Suyalatu, N. Nakamoto, N. Joko, Y. Nomura, S. Tsutsumi, H. Migita, S. Doi, A. Kurosu, N. Chiba, Y. Wakabayashi, T. Igarashi, Hanawa, microstructures and mechanical properties of Co-29Cr-6Mo alloy fabricated by selective laser melting process for dental applications, J. Mech. Behav. Biomed. Mater. 21 (2013) 67–76.

[10] N.T. Aboulkhair, I. Maskery, C. Tuck, I. Ashcroft, N.M. Everitt, On the formation of AlSi10Mg single tracks and layers in selective laser melting: Microstructure and nano-mechanical properties, J. Mater. Process. Technol. 230 (2016) 88–98.

[11] H. Rao, S. Giet, K. Yang, X. Wu, C.H.J. Davies, The influence of processing parameters on aluminium alloy A357 manufactured by selective laser melting, Mater. Des. 109 (2016) 334–346.

[12] U. Tradowsky, J. White, R.M. Ward, N. Read, W. Reimers, M.M. Attallah, Selective laser melting of AlSi10Mg: influence of post-processing on the microstructural and tensile properties development, Mater. Des. 105 (2016) 212–222.

[13] N. Read, W. Wang, K. Essa, M.M. Attallah, Selective laser melting of AlSi10Mg alloy: process optimisation and mechanical properties development, Mater. Des. 65 (2015) 417–424.

[14] M.L. Montero Sistiaga, R. Mertens, B. Vrancken, X. Wang, B. Van Hooreweder, J.P. Kruth, J. Van Humbeeck, Changing the alloy composition of Al7075 for better processability by selective laser melting, J. Mater. Process. Technol. 238 (2016) 437–445.

[15] H. Zhang, H. Zhu, T. Qi, Z. Hu, X. Zeng, Selective laser melting of high strength Al-Cu-Mg alloys: processing, microstructure and mechanical properties, Mater. Sci. Eng. A 656 (2016) 47–54.

[16] H. Zhang, H. Zhu, X. Nie, J. Yin, Z. Hu, X. Zeng, Effect of zirconium addition on crack, microstructure and mechanical behavior of selective laser melted Al-Cu-Mg alloy, Scr. Mater. 134 (2017) 6–10.

[17] T. Qi, H. Zhu, H. Zhang, J. Yin, L. Ke, X. Zeng, Selective laser melting of Al7050 powder: melting mode transition and comparison of the characteristics between the keyhole mode and conduction mode, Mater. Des. 135 (2017) 257–266.

[18] N. Kaufmann, M. Imran, T.M. Wischeropp, C. Emmelmann, S. Siddique, F. Walther, Influence of process parameters on the quality of aluminium alloy en AW 7075 using selective laser melting (SLM), Phys. Procedia 83 (2016) 918–926.

[19] B. Ahuja, M. Karg, K.Y. Nagulin, M. Schmidt, Fabrication and characterization of high strength Al-Cu alloys processed using laser beam melting in metal powder bed, Phys. Procedia 56 (2014) 135–146.

[20] P. Wang, C. Gammer, F. Brenne, K.G. Prashanth, R.G. Mendes, M.H. Rümmeli, T. Gemming, J. Eckert, S. Scudino, Microstructure and mechanical properties of a heat-treatable Al-3.5Cu-1.5Mg-1Si alloy produced by selective laser melting, Mater. Sci. Eng. A 711 (2018) 562–570.

[21] J.H. Martin, B.D. Yahata, J.M. Hundley, J.A. Mayer, T.A. Schaedler, T.M. Pollock, 3D printing of high-strength aluminium alloys, Nature. 549 (2017) 365–369.

[22] J. Royset, Scandium in Aluminium alloys overview: physical metallurgy, properties and applications, Metall. Sci. Technol. 25 (2007) 11–21.

[23] V.G. Davydov, T.D. Rostova, V.V. Zakharov, Y.A. Filatov, V.I. Yelagin, Scientific principles of making an alloying addition of scandium to aluminium alloys, Mater. Sci. Eng. A 280 (2000) 30–36.

[24] S. Costa, H. Puga, J. Barbosa, A.M.P. Pinto, The effect of Sc additions on the microstructure and age hardening behaviour of as cast Al-Sc alloys, Mater. Des. 42 (2012) 347–352.

[25] V.V. Zakharov, I.A. Fisenko, Alloying aluminum alloys with scandium, Met. Sci. Heat Treat. 59 (2017) 278–284.

[26] K. Schmidtke, F. Palm, A. Hawkins, C. Emmelmann, Process and mechanical properties: applicability of a scandium modified Al-alloy for laser additive manufacturing, Phys. Procedia 12 (2011) 369–374.

[27] Y. Shi, P. Rometsch, K. Yang, F. Palm, X. Wu, Characterisation of a novel Sc and Zr modified Al–Mg alloy fabricated by selective laser melting, Mater. Lett. 196 (2017) 347–350.

[28] H. Zhang, D. Gu, J. Yang, D. Dai, T. Zhao, C. Hong, A. Gasser, R. Poprawe, Selective laser melting of rare earth element Sc modified aluminum alloy: thermodynamics of precipitation behavior and its influence on mechanical properties, Addit. Manuf. 23 (2018) 1–12.

[29] R. Li, M. Wang, T. Yuan, B. Song, C. Chen, K. Zhou, P. Cao, Selective laser melting of a novel Sc and Zr modified Al-6.2 Mg alloy: Processing, microstructure, and properties, Powder Technol. 319 (2017) 117–128.

[30] R. Li, H. Chen, H. Zhu, M. Wang, C. Chen, T. Yuan, Effect of aging treatment on the microstructure and mechanical properties of Al-3.02Mg-0.2Sc-0.1Zr alloy printed by selective laser melting, Mater. Des. 168 (2019) 107668.

[31] A.B. Spierings, K. Dawson, M. Voegtlin, F. Palm, P.J. Uggowitzer, Microstructure and mechanical properties of as-processed scandium-modified aluminium using selective laser melting, CIRP Ann. -Manuf. Technol. 65 (2016) 213–216.

[32] A.B. Spierings, K. Dawson, T. Heeling, P.J. Uggowitzer, R. Schäublin, F. Palm, K. Wegener, Microstructural features of Sc- and Zr-modified Al-Mg alloys processed by selective laser melting, Mater. Des. 115 (2017) 52–63.

[33] A.B. Spierings, K. Dawson, K. Kern, F. Palm, K. Wegener, SLM-processed Sc- and Zr-modified Al-Mg alloy: mechanical properties and microstructural effects of heat treatment, Mater. Sci. Eng. A 701 (2017) 264–273.

[34] A.B. Spierings, K. Dawson, P.J. Uggowitzer, K. Wegener, Influence of SLM scan-speed on microstructure, precipitation of Al3Sc particles and mechanical properties in Sc- and Zr-modified Al-Mg alloys, Mater. Des. 140 (2018) 134–143.

[35] Q. Jia, P. Rometsch, S. Cao, K. Zhang, X. Wu, Towards a high strength aluminium alloy development methodology for selective laser melting, Mater. Des. 174 (2019) 107775.

[36] Q. Jia, P. Rometsch, P. Kürnsteiner, Q. Chao, A. Huang, M. Weyland, L. Bourgeois, X. Wu, Selective laser melting of a high strength Al-Mn-Sc alloy: alloy design and strengthening mechanisms, Acta Mater. 171 (2019) 108–118.

[37] N.T. Aboulkhair, N.M. Everitt, I. Maskery, I. Ashcroft, C. Tuck, Selective laser melting of aluminum alloys, MRS Bull. 42 (2017) 311–319.

[38] L. Thijs, K. Kempen, J.P. Kruth, J. Van Humbeeck, Fine-structured aluminium products with controllable texture by selective laser melting of pre-alloyed AlSi10Mg powder, Acta Mater. 61 (2013) 1809–1819.

[39] A. Yadollahi, N. Shamsaei, Additive manufacturing of fatigue resistant materials: challenges and opportunities, Int. J. Fatigue 98 (2017) 14–31.

[40] N. Shamsaei, J. Simsiriwong, Fatigue behaviour of additively-manufactured metallic parts, Procedia Struct. Integr. 7 (2017) 3–10.

[41] A.B. Spierings, M. Schneider, R. Eggenberger, Comparison of density measurement techniques for additive manufactured metallic parts, Rapid Prototyp. J. 17 (2011) 380–386.

[42] J. Shi, S. Ma, S. Wei, J.P. Best, M. Stolpe, A. Beckmann, S. Mostafavi, S. Korte-Kerzel, B. Markert, 3D pore structure characterization and hardness in a powder bed fusion-processed fully amorphous Zr-based bulk metallic glass, Mater. Charact. 162 (2020) 110178.

[43] C.A. Schneider, W.S. Rasband, K.W. Eliceiri, NIH image to ImageJ: 25 years of image analysis, Nat. Methods 9 (2012) 671–675.

[44] I. Maskery, N.T. Aboulkhair, M.R. Corfield, C. Tuck, A.T. Clare, R.K. Leach, R.D. Wildman, I.A. Ashcroft, R.J.M. Hague, Quantification and characterisation of porosity in selectively laser melted Al-Si10-Mg using X-ray computed tomography, Mater. Charact. 111 (2016) 193–204.

[45] C.Y. Yap, C.K. Chua, Z.L. Dong, Z.H. Liu, D.Q. Zhang, L.E. Loh, S.L. Sing, Review of selective laser melting: materials and applications, Appl. Phys. Rev. 2 (2015), 041101, .

[46] X. Han, H. Zhu, X. Nie, G. Wang, X. Zeng, Investigation on selective laser melting AlSi10Mg cellular lattice strut: Molten pool morphology, surface roughness and dimensional accuracy, Materials (Basel). 11 (2018) 392.

[47] J. Zhang, B. Song, Q. Wei, D. Bourell, Y. Shi, A review of selective laser melting of aluminum alloys: processing, microstructure, property and developing trends, J. Mater. Sci. Technol. 35 (2019) 270–284.

[48] K.V. Yang, P. Rometsch, T. Jarvis, J. Rao, S. Cao, C. Davies, X. Wu, Porosity formation mechanisms and fatigue response in Al-Si-Mg alloys made by selective laser melting, Mater. Sci. Eng. A 712 (2018) 166–174.

[49] M.R. Alkahari, T. Furumoto, T. Ueda, A. Hosokawa, R. Tanaka, M.S. Abdul Aziz, Thermal conductivity of metal powder and consolidated material fabricated via selective laser melting, Key Eng. Mater. 523–524 (2012) 244–249.

[50] Y. Shi, K. Yang, S.K. Kairy, F. Palm, X. Wu, P.A. Rometsch, Effect of platform temperature on the porosity, microstructure and mechanical properties of an Al–Mg–Sc–Zr alloy fabricated by selective laser melting, Mater. Sci. Eng. A 732 (2018) 41–52.

[51] I. Polmear, D.St. John, J.F. Nie, M. Qian, Light Alloys: Metallurgy of the Light Metals, fifth ed. Elsevier, Oxford, 2017.

[52] S. Zhou, Z. Zhang, M. Li, D. Pan, H. Su, X. Du, P. Li, Y. Wu, Correlative characterization of primary particles formed in as-cast Al-Mg alloy containing a high level of Sc, Mater. Charact. 118 (2016) 85–91.

[53] K.V. Yang, Y. Shi, F. Palm, X. Wu, P. Rometsch, Columnar to equiaxed transition in Al-Mg(-Sc)-Zr alloys produced by selective laser melting, Scr. Mater. 145 (2018) 113–117.

[54] S. Iwamura, Y. Miura, Loss in coherency and coarsening behavior of Al3Sc precipitates, Acta Mater. 52 (2004) 591–600.

[55] A.F. Norman, P.B. Prangnell, R.S. McEwen, The solidification behaviour of dilute aluminium-scandium alloys, Acta Mater. 46 (1998) 5715–5732.

[56] K.B. Hyde, A.F. Norman, P.B. Prangnell, The effect of cooling rate on the morphology of primary Al3Sc intermetallic particles in Al-Sc alloys, Acta Mater. 49 (2001) 1327–1337.

[57] R. Ma, C. Peng, Z. Cai, R. Wang, Z. Zhou, X. Li, X. Cao, Effect of bimodal microstructure on the tensile properties of selective laser melt Al-Mg-Sc-Zr alloy, J. Alloys Compd. 815 (2020) 152422.

[58] J. Glerum, T. Sun, C. Kenel, D.C. Dunand, Synthesis of precipitation-strengthened Al-Sc, Al-Zr and Al-Zr-Sc alloys via selective laser melting of elemental powder blends, Submitt. Addit. Manuf. 101461 (2020).

[59] J.R. Davis, Aluminum and Aluminum Alloys, ASM International, 1994.

[60] D. Shechtman, R.J. Schaefer, F.S. Biancaniello, Precipitation in rapidly solidified Al-Mn alloys, Metall. Trans. A, Phys. Metall. Mater. Sci. 15 A (1984) 1987–1997.

[61] Ø. Ryen, O. Nijs, E. Sjölander, B. Holmedal, H.E. Ekström, E. Nes, Strengthening mechanisms in solid solution aluminum alloys, Metall. Mater. Trans. A Phys. Metall. Mater. Sci. 37 (2006) 1999–2006.

[62] D. Shechtman, I. Blech, D. Gratias, J.W. Cahn, Metallic phase with long-range orientational order and no translational symmetry, Phys. Rev. Lett. 53 (1984) 1951–1953.

[63] K. Stan-Głowińska, Ł. Rogal, A. Góral, A. Wierzbicka-Miernik, J. Wojewoda-Budka, N. Schell, L. Lityńska-Dobrzyńska, Formation of a quasicrystalline phase in Al–Mn base alloys cast at intermediate cooling rates, J. Mater. Sci. 52 (2017) 7794–7807.

[64] D. Pavlyuchkov, S. Balanetskyy, W. Kowalski, M. Surowiec, B. Grushko, Stable decagonal quasicrystals in the Al-Fe-Cr and Al-Fe-Mn alloy systems, J. Alloys Compd. 477 (2009) L41–L44.

[65] S. Balanetskyy, D. Pavlyuchkov, T. Velikanova, B. Grushko, The Al-rich region of the Al-Fe-Mn alloy system, J. Alloys Compd. 619 (2015) 211–220.

[66] P. Cao, M. Qian, D.H. Stjohn, Effect of manganese on grain refinement of Mg-Al based alloys, Scr. Mater. 54 (2006) 1853–1858.

[67] S. Pedrazzini, M. Galano, F. Audebert, D.M. Collins, F. Hofmann, B. Abbey, A.M. Korsunsky, M. Lieblich, A. Garcia Escorial, G.D.W. Smith, Strengthening mechanisms in an Al-Fe-Cr-Ti nano-quasicrystalline alloy and composites, Mater. Sci. Eng. A 672 (2016) 175–183.

[68] A. Inoue, H. Kimura, S.I. Yamaura, Production and mechanical properties of aluminum alloys with dispersed nanoscale quasicrystalline and amorphous particles, Met. Mater. Int. 9 (2003) 527–536.

[69] Z. Wang, X. Lin, N. Kang, Y. Hu, J. Chen, W. Huang, Strength-ductility synergy of selective laser melted Al-Mg-Sc-Zr alloy with a heterogeneous grain structure, Addit. Manuf. 34 (2020) 101260.